

# Shock wave driven by a phased implosion

R. Menikoff, K. S. Lackner, N. L. Johnson, S. A. Colgate, and J. M. Hyman  
*Theoretical Division, Los Alamos National Laboratory, Los Alamos, New Mexico 87545*

G. A. Miranda

*Dynamic Testing Division, Los Alamos National Laboratory, Los Alamos, New Mexico 87545*

(Received 24 April 1990; accepted 20 September 1990)

In this paper the theory of an axially phased radial implosion of a channel is developed. When the phase velocity of the implosion exceeds the sound velocity inside the channel, a planar shock wave traveling along the channel axis can develop. For the energy of the implosion system in the appropriate range, the theory predicts a stable steady-state flow configuration. The effect of the phased implosion is for the channel wall to form a nozzle that travels along the channel axis. The flow behind the axial shock is well described by the equations for nozzle flow with an additional dynamical degree of freedom for the shape of the wall. Experiments presented here verify the theoretical predictions. The numerical simulations show the formation of the axial shock during start-up and the approach to steady state to be in good agreement with experiment and theory. A potential application of the axially phased implosion is the design of a super shock tube.

## I. INTRODUCTION

An axially phased implosion of a channel can act as a "virtual" piston to drive a planar shock wave in a working fluid within the channel. The implosion pinches off the channel while the axial phasing causes the constricted region to travel along the channel as depicted in Fig. 1. Energy is concentrated in shock compressed fluid within the channel by collecting the energy from the implosion along the length of the channel. This concept was introduced in Refs. 1 and 2, and used with a high explosive drive for the phased implosion to develop a high powered gas gun.

The formation of an axial shock wave using a virtual piston requires that the axial phase velocity exceeds the sound speed of the working fluid. Furthermore, the implosion must be strong enough to collapse the channel wall to the axis. When the wall does not reach the axis the supersonically phased implosion acts as a leaky piston or peristaltic pump, which nevertheless can drive a shock along the channel.

In this paper, we focus on the case in which the flow through the leaky piston reaches steady state. In a frame comoving with the phased implosion, the flow in the channel reduces to the flow in a nozzle that is well described by the one-dimensional equations for duct flow. However, unlike in the standard duct flow, the shape of the duct itself becomes a dynamical degree of freedom.

Phased implosions can be used in shock tube applications to reach extreme pressures and energy densities. With high explosives driving the implosion, a very strong axial shock wave can be generated. The implosion also serves to confine the high pressure that cannot be contained by material strength. Such a system can be viewed as a super shock tube.

Our goal in this paper is threefold: to describe the theory of a steady-state axial shock driven by a phased implosion, to present the experiments that verify this theory, and to show

numerical calculations that simulate the initial development of the axial shock and the approach to steady state.

We begin our analysis in Sec. II by formulating the equations that model the flow in the working fluid inside the channel. The model equations are equivalent to those for one-dimensional fluid flow in a duct where the cross-sectional area is another dynamical variable and varies in both distance and time. The cross-sectional area is in part determined by an external traveling pressure pulse, which serves to drive the phased implosion and is applied to the outside of the channel wall.

The steady-state solution is characterized by a shock traveling at the phase velocity followed by an isentropic nozzle flow. An important feature of nozzle flow is that the fluid is sonic at the nozzle throat thereby decoupling the converging nozzle region from the flow behind (see Fig. 2). The

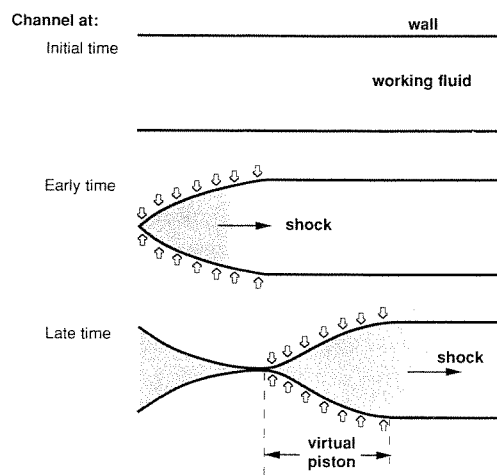


FIG. 1. Sketch of the time sequence of events in a phased channel implosion that acts as a "virtual" piston.

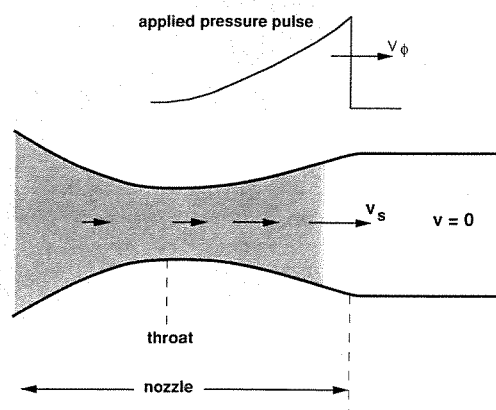


FIG. 2. Sketch of steady-state nozzle formed by phased implosion.

shape of the nozzle and the relative position of the axial shock adjust to the profile and strength of the applied pressure pulse. For the systems we consider, this axial shock is near the onset of the applied pressure pulse. Considerations of the energy balance between the work done by the applied pressure and the energy flow through the back of the nozzle show that the steady-state flow is stable.

Section III describes a simple explosively driven phased implosion experiment in which a nozzle flow approaching steady state actually occurs. The experimental apparatus consists of a cylindrical metal tube filled with *n*-hexane and surrounded by high explosives as shown in Fig. 3. A detonation wave travels along the axial direction of the tube and drives the phased implosion. Measurement of the shock planarity with a smear camera and the shape of the shock tube from a flash x ray confirm that a planar axial shock was formed and propagated.

Two-dimensional numerical calculations simulating the experiment are presented in Sec. IV. The calculations show the details of the formation of the axial shock and the approach to an asymptotic steady state. The results compare well with the experimental data but indicate that the experiment had not quite reached the steady state. The numerical calculation, extended over a longer distance of run, con-

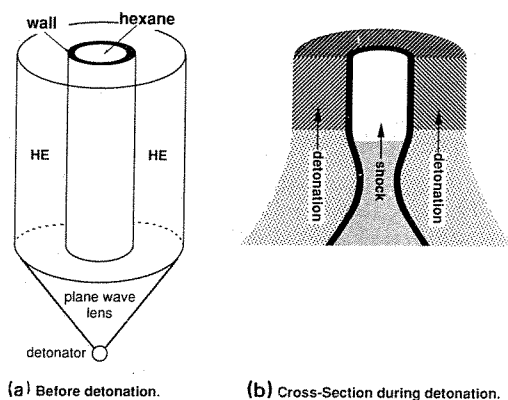


FIG. 3. Sketch of the explosively driven phased implosion experiment.

verged very accurately to the steady-state nozzle solution. This strongly indicates that the steady-state nozzle solution is the stable fixed point for fluid flow driven by phased implosions, provided that the energy balance allows the shock to ride near the onset of the pressure pulse.

In Sec. V we summarize the major points and discuss our results and potential applications of super shock tubes.

## II. THEORETICAL MODEL OF THE AXIAL SHOCK

From the general description of three-dimensional hydrodynamical equations we develop a one-dimensional approximation of the fluid flow in a cylindrical shock tube driven by a supersonically phased pressure pulse. We begin by introducing the notation. Let  $r$  and  $z$  be the radial and axial coordinates, and  $t$  the time. We denote the ambient conditions with the subscript 0. The flow of the working fluid and the wall material of the shock tube is described by the compressible fluid equations

$$\partial_t \rho + \nabla \cdot (\rho \mathbf{u}) = 0, \quad (1)$$

$$\partial_t (\rho \mathbf{u}) + \nabla \cdot (\rho \mathbf{u} \otimes \mathbf{u}) + \nabla P = 0, \quad (2)$$

$$\partial_t (\rho \mathcal{E}) + \nabla \cdot (\rho \mathcal{E} \mathbf{u}) + \nabla \cdot (P \mathbf{u}) = 0, \quad (3)$$

where  $\rho$  is the mass density,  $\mathbf{u}$  is the particle velocity,  $\mathcal{E} = \frac{1}{2} |\mathbf{u}|^2 + E$  is the total specific energy,  $E$  is the specific internal energy,  $P$  is the pressure, and  $V = 1/\rho$  is the specific volume. We use  $u$  and  $v$  for the radial and axial component of  $\mathbf{u}$  and  $S$  for the specific entropy. The working fluid and wall are distinguished by their equation of state  $P(V, E)$ .

The implosion system is modeled by a boundary condition; an applied pressure pulse on the outside of the shock tube wall traveling at a constant axial phase velocity  $v_\phi$ ,

$$P_a(z, t) = \tilde{P}_a(t - z/v_\phi). \quad (4)$$

The applied pressure profile  $\tilde{P}_a(t)$  is  $P_0$  for  $t < 0$ , rises abruptly at  $t = 0$ , and then falls monotonically to  $P_0$  for  $t > 0$ . The point  $z = v_\phi t$  is referred to as the onset of the applied pressure pulse. For this paper the phase velocity is supersonic relative to the ambient state of the working fluid,  $v_\phi > c_0$ .

### A. Qualitative description

To define a framework for our analysis and to justify our later approximations we give a short, qualitative description of the flow generated by a phased implosion of a cylindrical shock tube. The description follows the flow from the formation to the asymptotic steady-state propagation of an axial shock in the working fluid within the shock tube.

The wall motion at the start of the phased implosion creates a shock in the working fluid oblique to the axis. Due to the cylindrical convergence, the slope  $dr/dz$  of the shock front steepens and the reflection on axis results in a Mach configuration (see Fig. 4). As the wall continues to implode, the radial compression of the fluid creates an axial pressure gradient that leads to a compression wave behind the Mach configuration. The interaction of the compression wave with the Mach configuration strengthens the Mach stem and causes the triple point to move radially outward. The Mach stem grows in radial extent and becomes the axial shock.

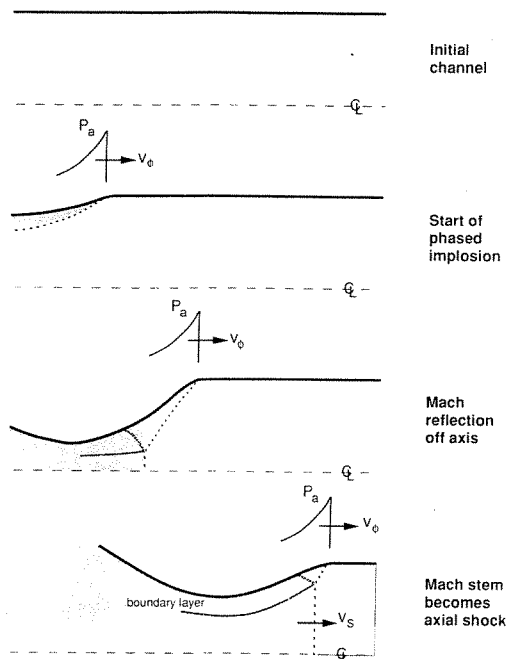


FIG. 4. Sketch of the time sequence of events leading to the formation of an axial shock.

During this initial phase, the wall implodes inward by a large fraction of the tube radius. Due to the low initial pressure in the working fluid, most of the energy supplied by the applied pressure pulse is converted into kinetic energy of the wall. The wall inertia and the applied pressure drive the wall inward until the radial compression of the working fluid leads to a sufficiently high internal pressure to decelerate and then reverse the wall motion. If the applied pressure pulse supplies sufficient energy, then the compression of the fluid will be large enough for its characteristic velocity to exceed the phase velocity,  $c + v > v_0$ . This is a necessary criterion for the compression wave to catch up with and strengthen the Mach configuration. Otherwise, when the applied pressure pulse is weak, the compression wave remains behind the phased implosion and the resulting flow pattern consists merely of a weak oblique shock and its reflections off the axis and wall.

When the speed of the compression wave exceeds the phase velocity, the pressure behind the axial shock increases. This increases the work the wall does on the fluid and further amplifies the fluid pressure until it is limited by the energy available from the applied pressure. The higher fluid pressure decreases the net force across the wall and thus decreases its inward acceleration. Once the axial shock propagates near the onset of the applied pressure pulse, the inward motion of the wall is substantially smaller than during formation of the axial shock.

The energy from the applied pressure pulse does  $P dV$  work on the fluid. During startup  $P$  is small and  $dV$  is large. Once an axial shock has formed,  $P$  is large and  $dV$  is small. The balance between the energy supplied by the applied pressure pulse and the energy absorbed by the working fluid causes the axial shock to asymptotically approach a steady state. This process is described next.

## B. One-dimensional model

Two approximations are needed to obtain a simple one-dimensional model of the phased implosion of a shock tube. The first neglects the axial motion and internal structure of the wall; the second neglects the radial velocity and radial dependence of variables within the working fluid. Both approximations require that the phase velocity be much larger than the wall velocity. The experiments and numerical calculations presented later confirm that these approximations are valid for a wide range of conditions.

### 1. Thin wall approximation

When the shock tube wall is sufficiently thin, the transit time for a radial signal in the wall is short compared to the transit time for a radial signal in the working fluid. Therefore, to analyze the fluid flow inside the shock tube, we can approximate the shock tube wall with a mass layer and characterize the wall with its mass per unit length  $\sigma$  and its radius  $R(z, t)$ . Radial shocks and internal energy in the wall are neglected. We also assume that  $P_a$  is much larger than the yield strength of the wall and neglect its material strength.

With these approximations, the motion of the shock tube wall is governed by Newton's law

$$\sigma \frac{\partial^2 R}{\partial t^2} = 2\pi R(z, t) [P(R, z, t) - P_a(z, t)]. \quad (5)$$

Implicit in this equation is that the force on the wall is directed radially, which requires  $|dR/dz| \ll 1$ . This condition is valid when  $\sigma$  is large enough for the wall velocity to remain small relative to the phase velocity. Once the axial shock is formed this condition on  $\sigma$  is easily satisfied because the pressure difference across the wall tends to be small.

### 2. Reduction to one dimension

When the ratio of the radial wall velocity to the axial phase velocity is small, then  $|dR/dz| \ll 1$  and the sound speed behind the axial shock will be large compared to the wall velocity. Under these conditions, it is a good approximation to neglect the radial velocity and the radial dependence of the flow inside the shock tube, see e.g., Ref. 3. Equations (1)–(3) for the fluid flow reduce to the equations for one-dimensional (1-D) flow in a duct of variable and time-dependent cross-sectional area,  $A = \pi R^2$ :

$$\partial_t(\rho A) + \partial_z(\rho A v) = 0, \quad (6)$$

$$\partial_t(\rho A v) + \partial_z(\rho A v^2 + P A) = P \partial_z A, \quad (7)$$

$$\partial_t(\rho A \mathcal{E}) + \partial_z(\rho A \mathcal{E} v + P A v) = -P \partial_z A. \quad (8)$$

The variation of  $A$  with  $z$  retains the most important aspects to the two-dimensional flow. The cross-sectional area is coupled to the fluid pressure inside the duct by the wall equation of motion, Eq. (5). Consequently, the shape of the duct is a dynamical degree of freedom.

Equations (5)–(8) represent the one-dimensional model for the phased implosion of the shock tube. There are several important points to note on the structure of the model equations. The right-hand side of Eqs. (7) and (8) are source terms for the 1-D axial fluid flow. Equation (5) allows for a discontinuity in the radial wall acceleration, but

the radial wall velocity as well as  $R$  and  $A$  are always continuous. Furthermore, from the left-hand side of Eqs. (6)–(8) the mass, momentum, and energy densities and their fluxes are all proportional to  $A$ . Therefore  $A$  and the source terms do not effect the shock jump relations for the fluid flow. For the full fluid dynamics equations, Eqs. (1)–(3), the applied pressure is a boundary condition. But for the 1-D model the applied pressure enters Eq. (5) as a source term. Because the source is moving,  $v_\phi$  has the effect of an additional characteristic velocity.

The one-dimensional model equations do not accurately describe the formation of the axial shock because radial effects and, in particular, oblique radial shocks are important. However, after the axial shock has formed, the fluid behind it is on a high adiabat compared to the ambient conditions. The sound speed in the fluid is comparable to the phase velocity and hence large compared to the wall velocity. Consequently, the limited wall motion results in weak radial waves that have only a small effect on the fluid adiabat, and the model equations accurately describe the flow behind the axial shock.

Even after the axial shock has formed, the 1-D model equations (6)–(8) only apply to the region behind the shock. We approximate the fluid state in front of the axial shock by the ambient state. This neglects the radial structure that forms in front of the Mach stem when it rides behind the onset of the pressure pulse. In front of the Mach stem, sound velocities are small compared to the wall velocity and the radial waves are strong perturbations of the ambient state. However, the radial waves are confined to a narrow boundary layer near the wall if the axial shock is not riding too far behind the onset of the pressure pulse. Outside the boundary layer, the material in front of the shock remains in its ambient state.

This is in contrast to the precompression that would occur if Eqs. (6)–(8) were applied in front of the axial shock. This compression would change the initial state and hence the state behind the shock. For the same shock velocity, the flow rate and pressure behind the axial shock would be too high. Our formulation of the 1-D model gives the same pressure for the axial shock as for the Mach stem in the true flow. We are in effect, neglecting the flow between the wall and contact behind the Mach configuration (see Fig. 4). Hence this “boundary layer” region must be small for Eqs. (6)–(8) to be a good approximation and the applied pressure pulse must supply sufficient energy such that the radius  $R_s$  of the shock tube at the axial shock front is close to the initial radius,  $R_s \approx R_0$ .

### 3. Steady-state nozzle flow

We refer to the reference frame moving with the phase velocity  $v_\phi$  as the comoving frame. At steady state in the comoving frame, the axial shock is stationary and the shock tube wall has the shape of a converging–diverging nozzle. This configuration is sketched in Fig. 5. The radial flow can be neglected for a slender nozzle for which the length is long compared to the radius, and the ratio of the minimum radius to the initial radius is not too small. We are mainly interested in the flow in the converging section of the nozzle, i.e., be-

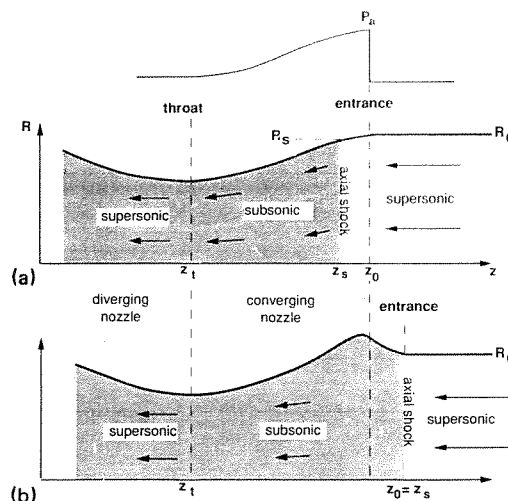


FIG. 5. Sketch of steady-state phased implosion in the comoving frame. (a) Shock behind the onset of pressure pulse. (b) Shock ahead of the onset of pressure pulse.

tween the entrance point at which the cross-sectional area first changes and the nozzle throat at which the cross-sectional area is minimum. The entrance point corresponds to the first motion of the wall; the onset of the applied pressure pulse or the position of the axial shock, whichever is ahead. When the applied pressure behind the nozzle throat is low compared to the axial shock pressure, i.e.,  $P_a$  falls off sufficiently fast, the flow in the converging section of the nozzle is unsupported from behind and is sonic at the nozzle throat. Thus the flow into the throat decouples from the flow behind. We denote the nozzle entrance by  $z_0$  and the nozzle throat by  $z_t$ .

The fluid equations (6)–(8) are invariant under Galilean transformations and have the same form in the comoving frame as in the lab frame. At steady state, in the comoving frame the wall is stationary and the source term on the right-hand side of Eq. (8) vanishes. Its effect is accounted for by the change in the kinetic energy under the Galilean transformation.

In the comoving frame at steady state, Eqs. (6)–(8) applied to the flow behind the axial shock reduce to the algebraic equations for nozzle flow, see e.g., Ref. 4. Let  $q = v_\phi - v$  be the velocity in the comoving nozzle frame:

$$\begin{aligned} \rho q A &= \text{const}, & \text{flow rate,} \\ \frac{1}{2} q^2 + E + PV &= \text{const}, & \text{Bernoulli's law,} \\ S &= \text{const}, & \text{isentropic flow.} \end{aligned}$$

The constants for the nozzle flow equations are determined by the state immediately behind the stationary shock with the particle velocity ahead of the shock equal in magnitude to the phase velocity  $v_\phi$ . Variables describing this state are denoted by the subscript  $s$ . In particular,  $z_s$  is the position of the shock and  $R_s$  is the radius of the shock tube at the shock front. The solution to the algebraic equations determines the flow variables  $\rho$ ,  $q$ ,  $E$ , and  $P$  as functions of the cross-sectional area ratio  $A/A_s$ , where  $A_s = \pi R_s^2$  is the area of the shock front. We denote this nozzle flow solution with the subscript  $N$ .

For a steady nozzle flow the area must always be above a critical value  $A_*$  determined by the fluid state and area at the nozzle entrance. There are two solutions to the nozzle flow equations for  $A > A_*$  corresponding to subsonic and supersonic flow (see Fig. 6). At the critical area the two branches meet in a sonic point of the flow. Because the flow behind a shock is subsonic, the flow between the axial shock and the nozzle throat corresponds to the subsonic branch of the nozzle flow in which  $P$  decreases with decreasing  $A$ . When the flow through the nozzle is transonic, the flow behind the nozzle throat is supersonic and corresponds to the branch of the nozzle flow in which  $P$  decreases with increasing  $A$ .

In the comoving frame, the steady-state shape of the wall depends on  $\tilde{P}_a$ . The wall shape  $R(z)$  at  $t = 0$  is determined by solving a pair of ordinary differential equations obtained by substituting the nozzle flow solution into Eq. (5). Note, in steady state  $\partial_t = -v_\phi \partial_z$ . Let  $U = \partial_t R$  be the radial wall velocity. Equation (5) can then be expressed as

$$v_\phi \frac{dR}{dz} = -U, \quad (9)$$

$$\sigma v_\phi \frac{dU}{dz} = -2\pi R \left[ P(z) - \tilde{P}_a \left( -\frac{z}{v_\phi} \right) \right], \quad (10a)$$

where

$$P(z) = \begin{cases} P_0, & \text{for } z_s < z, \\ P_N^{\text{sub}}(A(z)/A_s), & \text{for } z_i \leq z \leq z_s, \\ P_N^{\text{super}}(A(z)/A_s), & \text{for } z < z_i, \end{cases} \quad (10b)$$

and  $A = \pi R^2$ .

The boundary conditions are as follows. At the nozzle entrance the initial wall radius is  $R(z_0) = R_0$ , and the initial wall velocity is  $U(z_0) = 0$ . The nozzle throat is defined to occur at the minimum radius,  $U(z_i) = 0$  and  $R(z_i) < R_0$ . In addition, we require the flow at the nozzle to be sonic, i.e.,  $A(z_i) = A_*$ . We emphasize that the sonic condition depends on the equation of state and the nozzle flow equations but is independent of the applied pressure pulse.

The position of the axial shock  $z_s$  provides the extra

degree of freedom to satisfy the sonic condition at the nozzle throat. Thus  $z_s$  is similar to an eigenvalue. In Appendix A we show that there exists a solution and that it is unique. Physically, the position of the axial shock within the nozzle depends on the energy delivered to the working fluid by the applied pressure pulse. There are two cases. In the underdriven case, low external energy, the nozzle entrance coincides with the onset of  $\tilde{P}_a$ ,  $z_s < z_0$  and  $R_s < R_0$ , and the shock front is inside the converging section of the nozzle. In the overdriven case, large external energy, the nozzle entrance coincides with the shock front, which is ahead of the applied pressure pulse,  $R_s = R_0$  and  $z_0 = z_s$ , and the nozzle shape diverges outward before converging inward.

It is interesting to note that at steady state for  $z_s < z_0$ ,  $dP/dz < 0$  behind the shock front. For the transient during the formation of the axial shock,  $dP/dz > 0$  behind the Mach stem.

### C. Example of polytropic ideal gas

The purpose of this section is to illustrate the ideas developed in the previous section in the context of a concrete example. We begin by choosing an ideal polytropic equation of state for the working fluid,

$$P(V, E) = (\gamma - 1)E/V. \quad (11)$$

In Sec. II C 1 we parametrize the nozzle flow in terms of the variable  $V$ . In Sec. II C 2 we present an explicit analytic solution for the nozzle flow, which implies a particular form of the applied pressure pulse.

#### 1. The nozzle solution

When the strong-shock jump conditions apply ( $v_\phi \gg c_0$ ), the flow in the nozzle can be determined analytically. The state behind a stationary strong shock with upstream particle velocity  $v_\phi$  is

$$\begin{aligned} V_s &= [(\gamma - 1)/(\gamma + 1)]V_0, \\ P_s &= [2/(\gamma + 1)]\rho_0 v_\phi^2, \\ E_s &= [2/(\gamma + 1)^2]v_\phi^2, \\ q_s &= [(\gamma - 1)/(\gamma + 1)]v_\phi. \end{aligned} \quad (12)$$

The algebraic nozzle flow equations with this state as initial condition have the following solution parametrized by  $V$ :

$$\begin{aligned} P &= (V_s/V)^\gamma P_s, \\ E &= (V_s/V)^{\gamma-1} E_s, \\ q &= \{1 - [4\gamma/(\gamma + 1)^2](V_s/V)^{\gamma-1}\}^{1/2} v_\phi, \\ A &= (q_s V/q V_s) A_s. \end{aligned} \quad (13)$$

The sonic point is determined by the condition  $c^2 = \gamma PV = q^2$ . Solving for  $V$  we obtain

$$V_*/V_s = [2\gamma/(\gamma + 1)]^{1/(\gamma-1)}. \quad (14)$$

The other variables at the critical state for the nozzle flow are given by

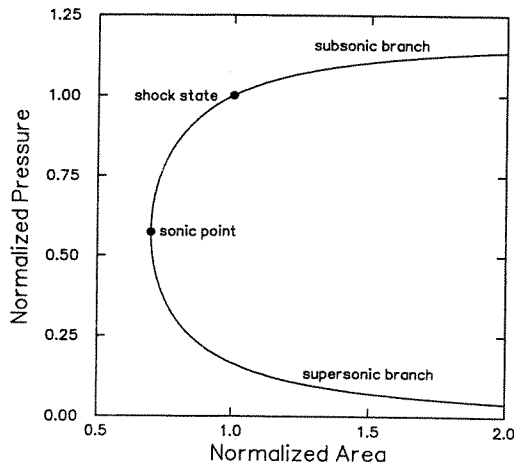


FIG. 6. Pressure versus area for an ideal gas with  $\gamma = 5/3$ .

$$\begin{aligned}
P_*/P_s &= [(\gamma + 1)/2\gamma]^{1/(\gamma-1)}, \\
E_*/E_s &= (\gamma + 1)/2\gamma, \\
\left(\frac{q_*}{v_\phi}\right)^2 &= \left(\frac{c_*}{v_\phi}\right)^2 = \frac{\gamma-1}{\gamma+1}, \\
\frac{A_*}{A_s} &= \left(\frac{\gamma-1}{\gamma+1}\right)^{1/2} \left(\frac{2\gamma}{\gamma+1}\right)^{1/(\gamma-1)}.
\end{aligned} \tag{15}$$

From Eq. (13),  $P$ ,  $E$ , and  $q$  vary monotonically with  $V$  while  $A$  is double valued. The subsonic branch corresponds to  $[2/(\gamma + 1)]^{1/(\gamma-1)} V_* < V < V_*$ , and the supersonic branch to  $V_* < V < \infty$ . As  $A \rightarrow \infty$ , the subsonic branch goes to  $q = 0$  and finite  $P$ , while the supersonic branch goes to  $\rho = 0$ ,  $P = 0$ , and finite  $q$ . On each branch Eq. (13) can easily be inverted numerically to give the variables as function of the area ratio  $A/A_s$ .

We note for steady-state propagation with the axial shock at the nozzle entrance, the wall implodes inward only a small fraction of the radius; for  $\gamma = \frac{5}{3}$ ,  $(R_0 - R_*)/R_0 = 1 - (A_*/A_0)^{1/2} = 17\%$ .

## 2. An analytic solution

Using Eqs. (12)–(15) we can construct a nontrivial exact steady-state solution for the 1-D model of the phased implosion, Eqs. (6)–(10), as follows. The solution is parametrized by  $V$ . The axial shock is at the nozzle entrance and the interval  $V_s \leq V \leq V_*$  corresponds to the subsonic region. We take the converging section of the nozzle to be the interval  $-L \leq z \leq 0$ .

The solution is determined by specifying a function for the axial coordinate  $z(V)$ . For example, let us choose

$$z(V) = -L [(V - V_s)/(V_* - V_s)]^{1/2}. \tag{16}$$

Since  $R(V)$  is already given by Eq. (13) the nozzle shape is determined. The wall velocity is determined by Eq. (9),

$$U(V) = -v_\phi \frac{dR}{dV} \left( \frac{dz}{dV} \right)^{-1}. \tag{17}$$

The function  $z(V)$  is chosen such that  $dz/dV \rightarrow \infty$  as  $V \rightarrow V_s$  in order for  $U$  to vanish at the nozzle entrance. The applied pressure pulse is determined by Eq. (10a),

$$\bar{P}_a \left( -\frac{z(V)}{v_\phi} \right) = P(V) + \frac{\sigma v_\phi}{2\pi R(V)} \frac{dU}{dV} \left( \frac{dz}{dV} \right)^{-1}. \tag{18}$$

By straightforward differentiation, and with  $P$ ,  $R$ , and  $q$  given by Eqs. (12) and (13),  $U$  and  $\bar{P}_a$  may be obtained analytically. The expressions are cumbersome to write out but easily evaluated numerically. In Fig. 7 this solution for  $P(z)$ ,  $\bar{P}_a(-z/v_\phi)$ , and  $R(z)$  is shown for a particular choice of parameters  $v_\phi$ ,  $\sigma$ ,  $R_0$ ,  $L$ ,  $\gamma$ ,  $V_0$ , and  $P_0$ . This solution extends into the supersonic region corresponding to  $V > V_*$ . The qualitative behavior of the variables in the general case is the same as for this example. This has been observed in experiments and numerical simulations (see Secs. III and IV).

## D. The energy balance

Next we consider the energy balance in the lab frame for the steady-state fluid flow in the converging section of the nozzle formed by the phased implosion. This is equivalent to

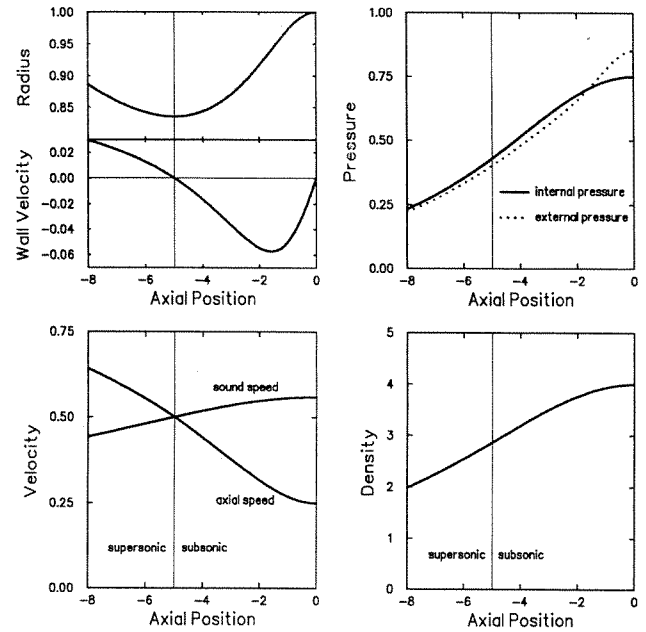


FIG. 7. Example of the exact steady-state nozzle solution ( $R_0 = 1$ ,  $L = 5$ ,  $\gamma = \frac{5}{3}$ ,  $\rho_0 = 1$ ,  $P_0 = 0$ ,  $\sigma = 10$ , and  $v_\phi = 1$ ): wall shape and radial velocity, internal and external pressure, axial speed and sound speed, and density.

deriving the analog of the Hugoniot jump conditions across the nozzle.

At steady state, either the axial coordinate, wall radius, or time may be used as the independent variable to parametrize the flow. The relation of these variables is most easily expressed in differential form,

$$dz = -v_\phi dt = -(v_\phi/U) dR. \tag{19}$$

Conservation of energy for the fluid may be expressed by integrating Eq. (8) across the length of the nozzle from  $z_i$  to  $z_0$ . With substitutions using Eq. (19), this can be expressed as

$$\begin{aligned}
&[\rho_0(v_0 - v_\phi)(\frac{1}{2}v_0^2 + E_0) + P_0 v_0] A_0 \\
&- [\rho_t(v_t - v_\phi)(\frac{1}{2}v_t^2 + E_t) - P_t v_t] A_t = v_\phi \int_{A_t}^{A_0} P dA,
\end{aligned} \tag{20}$$

where the subscripts 0 and  $t$  denote the nozzle entrance and throat, respectively.

Similarly, conservation of energy for the wall may be expressed by multiplying Eq. (10a) by  $U$  then integrating across the nozzle. By substituting Eq. (19) and  $U = 0$  at the nozzle entrance and throat we obtain

$$\int_{A_t}^{A_0} P dA = \int_{A_t}^{A_0} \bar{P}_a dA. \tag{21}$$

This equation results from neglecting the internal energy and the thickness of the wall. All the work done by the applied pressure on the wall is transferred to the fluid.

The average external work per unit length done on the shock tube is given by

$$\frac{\dot{E}_{\text{ext}}}{v_\phi} = \frac{E_{\text{ext}}}{\text{length}} = \int_{A_t}^{A_0} \bar{P}_a dA. \tag{22}$$

Combining Eqs. (20)–(22) we obtain the energy balance equation

$$[\rho_0(v_0 - v_\phi)(\frac{1}{2}v_0^2 + E_0) + P_0 v_0]A_0 - [\rho_i(v_i - v_\phi)(\frac{1}{2}v_i^2 + E_i) - P_i v_i]A_i = \dot{E}_{\text{ext}}. \quad (23)$$

The interpretation of this equation is that the rate of external work done on the nozzle is equal to the rate energy is lost out the back of the nozzle by the fluid flow.

Analog of the Hugoniot jump conditions across the nozzle can also be derived for mass and momentum. The nozzle jump condition for mass differs from the shock jump condition as a result of the change in area across the nozzle. For the momentum, the nozzle jump condition is also affected by a source term, the right-hand side of Eq. (7). Thus the applied pressure pulse supplies both energy and momentum to the fluid. The nozzle jump conditions reduce to the shock jump conditions when  $P_a$  vanishes and  $A_0 = A_i$ .

When the working fluid is described by an ideal polytropic equation of state the energy balance equation can be simplified. Assuming the strong shock limit, the incoming energy flux is small and the first term on the left-hand side of Eq. (23) may be neglected. Substituting Eq. (15) for the quantities at the nozzle throat into Eq. (23) and simplifying we obtain an expression for the external energy per unit length,

$$\frac{E_{\text{ext}}}{\text{length}} = \frac{\gamma + 1}{2\gamma} \left[ 1 - \left( \frac{\gamma - 1}{\gamma + 1} \right)^{1/2} \right]^2 \rho_0 v_\phi^2 A_s. \quad (24)$$

By comparison a piston driving a shock with the same shock velocity  $v_\phi$  would supply an energy,

$$E_{\text{piston}}/\text{length} = [2/(\gamma + 1)]\rho_0 v_\phi^2 A_0. \quad (25)$$

Thus a phased implosion requires a smaller amount of power to drive a shock at a fixed velocity than a piston; for example, when  $\gamma = \frac{5}{3}$  and  $A_s = A_0$  then  $\dot{E}_{\text{ext}}/\dot{E}_{\text{piston}} = 27\%$ . This is because the amount of fluid in a nozzle is fixed while the amount of fluid shocked by a piston increases. The phased implosion acts like a leaky piston or peristaltic pump to drive the axial shock. The advantage of the peristaltic pump over the virtual piston configuration is that a higher shock velocity can be achieved for a given power of the driving system.

## E. Stability considerations

### 1. Stability of model flow

We consider the stability of the flow for the 1-D model equations of the phased implosion, Eqs. (5)–(8). In the co-moving frame, the steady-state flow is the same as for a supersonic fluid entering a converging–diverging nozzle. The stationary axial shock is in the converging region of the nozzle for the undriven case, and at the entrance to a diverging region of the nozzle in the overdriven case. We contrast the stability of the flow generated by the phased implosion with the flow through a fixed nozzle.

A stability analysis of Eqs. (6)–(8) for a fixed nozzle shape,  $\partial_t A = 0$ , shows that a stationary shock is stable in a diverging section and unstable in a converging region of the nozzle.<sup>5–7</sup> Superficially this would suggest that the axial shock is unstable in the underdriven case. However, there are several significant differences that prevent the standard

nozzle stability analysis from applying to the axial shock formed by a phased implosion.

A critical difference between the channel flow generated by the phased implosion and the nozzle flow in the standard stability analysis is that the wall radius is an extra degree of freedom [Eq. (5)]. The shape of the nozzle is not fixed but adjusts to the flow inside. Another important difference is the boundary conditions for the nozzle flow. The upstream boundary is the ambient condition in front of the axial shock. For the axial shock inside the nozzle, this is motivated by the 2-D effects that give rise to oblique shocks and a Mach configuration. Because the flow is supersonic at the nozzle entrance, the state in front of the Mach stem is undisturbed and is the same as the incoming flow. For the axial shock near the nozzle entrance, the error in the mass flow is not significant.

In contrast, the standard boundary condition for the fixed nozzle stability analysis is a fixed inflow state at the nozzle entrance. This results in a radial precompression in front of the axial shock when the shock is in the converging section of the nozzle. An important destabilizing aspect of the precompression is that a higher shock pressure is needed for a stationary shock as it is moved deeper into the nozzle. The standard analysis also uses a fixed state as a downstream boundary condition. This is inappropriate for the phased implosion because of the interaction of the moving wall with the fluid flow; the appropriate downstream boundary is a sonic condition at the nozzle throat.

A shock in a converging section of a fixed nozzle either falls back and out the throat, or moves forward past the nozzle entrance. The analysis in Appendix A shows that the model equations for the phased implosion have a unique steady-state solution. The proof is based on the balance between the energy needed to propagate the flow ahead of the nozzle throat and the external energy supplied by the applied pressure pulse. The sign of the slope of the energy difference as a function of the axial shock position indicates that the steady-state flow formed by the phased implosion is stable.

Suppose the position of the axial shock is perturbed relative to the steady-state solution. If the shock were to move ahead then the applied pressure pulse would have insufficient energy to implode the wall down to the critical radius for steady-state nozzle flow. In addition, when  $P_a$  falls off sufficiently fast the flow is unsupported from behind and a rarefaction from the nozzle throat would overtake the shock and pull it back. On the other hand, if the shock were to move back then the applied pressure pulse would have sufficient energy to implode the wall past the critical radius. The flow in the nozzle would choke, and a compression wave formed at the nozzle throat would overtake the shock and push it forward. This is the 1-D version of the transient that initially forms the axial shock. Thus the interaction of the shock with the wall motion has a strong stabilizing effect on the fluid flow in the nozzle.

Similar arguments indicate that the steady state is also stable in the overdriven case in which the axial shock is ahead of the onset of the applied pressure pulse. The energy balance and uniqueness of the steady-state solution play an important role in the stability argument. We note that in



some circumstances another quasisteady asymptotic solution is possible. Suppose the working fluid density is sufficiently low, e.g., a gas, such that the axial shock pressure is below the yield strength of the wall and the nozzle flow is overdriven. A flow can occur in which the axial shock velocity is greater than the phase velocity. In this case the wall does not expand outward and the working fluid does not lose energy when the axial shock gets ahead of the applied pressure pulse. A quasisteady solution can be constructed. It consists of a steady nozzle flow preceded by a constant state region between the shock front and the onset of the pressure pulse that grows linearly with time. As the shock velocity increases above the phase velocity, the fluid will be on a higher adiabat and the constants for the algebraic flow equations will increase. Thus the wall can implode further toward the axis. The limiting case for the quasisteady solutions occurs when the particle velocity behind the shock is equal to the phase velocity and corresponds to the "virtual" piston concept previously considered in Refs. 1 and 2.

The stability argument discussed here is supported by the numerical calculations presented in Sec. IV. A mathematically rigorous analysis would involve linearizing Eqs. (5)–(8) about the steady-state solution and computing the growth rate of the normal modes. The linearized problem contains a free boundary, the position of the axial shock. The stability analysis would be very similar to that of a 1-D detonation wave. This is discussed further in Sec. V.

## 2. Stability under higher-dimensional perturbations

There is another aspect of fluid stability that is of concern for the phased implosion. This is the combined Rayleigh–Taylor and Kelvin–Helmholtz instability of the fluid–wall interface. For a rapidly imploding wall the yield strength of the wall is exceeded and one cannot rely on material strength to stabilize the interface. In the steady-state configuration the high pressure behind the axial shock limits the inward travel of the wall to a small fraction of the tube radius. The small radial convergence ratio results in a minimal growth of Rayleigh–Taylor instability. The growth of the Kelvin–Helmholtz instability starts at the nozzle entrance. The aspect ratio of the steady-state nozzle, the ratio of length to diameter, is an important factor. For an aspect ratio of order unity, the growth of a Kelvin–Helmholtz instability within the nozzle is small. In effect, the interface instability is minimal because the nozzle wall is continually fed new material and the old perturbed material is swept past the nozzle throat where it has no effect on the axial shock. The transit time for a fluid particle to pass through the nozzle sets the relevant time scale for the growth of instabilities. When the aspect ratio of the nozzle is small, there is insufficient time for the instability to develop to a significant amplitude.

Another 2-D instability involves the boundary layer that occurs when  $R_s < R_0$ . In this case the axial shock corresponds to the Mach stem of a Mach configuration where the stem extends nearly to the wall of the shock tube (see Fig. 4). Behind the Mach stem the flow is subsonic, while in the boundary layer behind the reflected shock of the Mach configuration the flow is supersonic. Across the contact between

the two regions, there is a velocity shear or vortex sheet that is subject to Kelvin–Helmholtz instability. Again, for small aspect ratios of the nozzle, the instabilities are swept out of the nozzle before significant growth occurs. We now show that, inside the nozzle, the vorticity across the contact surface actually decreases. The vorticity in the vortex sheet points in the azimuthal direction because the flow is symmetric about the cylindrical axis;

$$\nabla \times \mathbf{u} = \omega \hat{\theta}, \quad (26)$$

where  $\hat{\theta}$  is a unit vector in the azimuthal direction. The rate of change of the vorticity is given by

$$(\partial_t + \mathbf{u} \cdot \nabla) \omega = -(\nabla \cdot \mathbf{u}) \omega + (1/\rho^2) \nabla \rho \times \nabla P. \quad (27)$$

For the steady-state nozzle flow behind the axial shock, the source term  $\nabla \rho \times \nabla P$  decreases the vorticity along the contact. This decrease and the supersonic flow in the boundary layer have a stabilizing effect on the contact surface.

The subsonic flow behind the Mach stem and the supersonic flow in the boundary follow the two different branches of the nozzle flow equations. In order to stay in pressure equilibrium across the contact, the cross-sectional area of the boundary layer increases while the cross-sectional area of the flow behind the axial shock decreases. If the shock rides close to the onset of the pressure pulse then the boundary layer is small and this effect is not significant.

The effect of these surface instabilities is to add dissipation to the nozzle flow from either mixing of the boundary layer or wall friction. This can be compensated for by increasing the energy supplied by the applied pressure, otherwise, the shock will ride further back in the nozzle than is predicted by the zero dissipation limit.

## III. EXPLOSIVELY DRIVEN PHASED IMPLOSION EXPERIMENTS

We briefly describe a simple experiment in which an axial shock generated by a phased implosion is observed and measured. The experiment consists of a shock tube inside a cylinder of high explosive (HE). The HE is initiated at the end of the cylinder. The axially propagating detonation wave provides the applied pressure pulse that drives the phased implosion of the shock tube. A detailed description of this experiment and additional experiments are given in Refs. 8 and 9.

A drawing of the experiment (E-4933) is shown in Fig. 8. The working portion of the shock tube is 6.746 cm long by 0.856 cm i.d. ( $\frac{3}{8}$  in. o.d. with a 20 mil wall) for an aspect ratio of  $L/D = 7.9$ . It is surrounded to an outer diameter of 5.0 cm by PBX-9501, a high explosive that has a Chapman–Jouguet (CJ) detonation velocity of  $v_{\phi} = 0.88$  cm/ $\mu$ sec and a CJ pressure of 370 kbar. The working fluid in the shock tube is *n*-hexane,  $\rho_0 = 0.657$  g/cm<sup>3</sup>. The experiment is designed to be close to the energy limit for propagating an axial shock at the nozzle entrance, Eq. (23). With a lower working fluid density or additional HE energy, the axial shock would get ahead of the detonation front and send a precursor wave into the HE, unnecessarily complicating the analysis of the experiment.

The shape of the axial shock front and the detonation



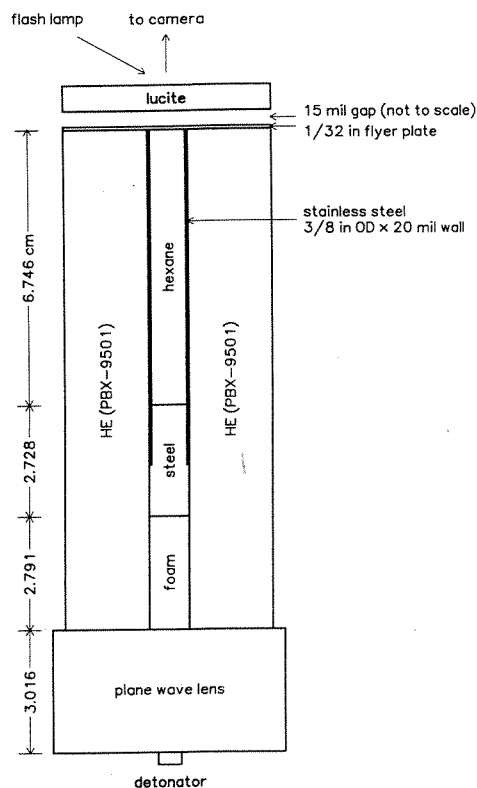


FIG. 8. Scale drawing of the hexane phased implosion experiment.

front are measured with the reflection-change/flying-flasher technique.<sup>10</sup> This technique enables the measurement of arrival times and shock strengths as follows. A thin air gap is sandwiched between a flyer plate and a transparent Lucite block. This assembly is placed at the end of the shock tube. The specially roughened free surface of the flyer plate is illuminated with a flash lamp and observed with a smear camera. The detonation wave in the HE or the axial shock in the hexane sends a transmitted shock into the flyer plate. The shock arriving at the surface changes the surface roughness, thereby changing the reflectance of the surface. Therefore the first change in intensity of the light marks the arrival of the shock at the free surface. Subsequently, the air gap is compressed and heated to incandescence by the motion of the flyer plate. Finally, the Lucite becomes opaque when it is hit by the flyer plate. Thus the impact of the flyer plate on the Lucite is marked by a bright flash. From the time difference between the reflectance change and the flash we can calculate the flyer plate velocity. The strength of the incident wave on the flyer plate is determined from the material equations of state by computing the shock impedance match backwards from the flyer plate velocity.

The time of the first motion of the free surface of the flyer plate and the arrival time of the flyer plate at the Lucite flasher as a function of radius are shown in Fig. 9. The inner portion of the flyer plate is driven by the axial shock in the hexane whereas the outer portion is driven by the detonation wave in the HE. The simultaneity of the reflection change of the light signal implies that the shock front in the hexane is flat to  $\pm 3$  nsec, ( $v_\phi \Delta t / D = \pm 0.003$ ) to within 0.05 cm of

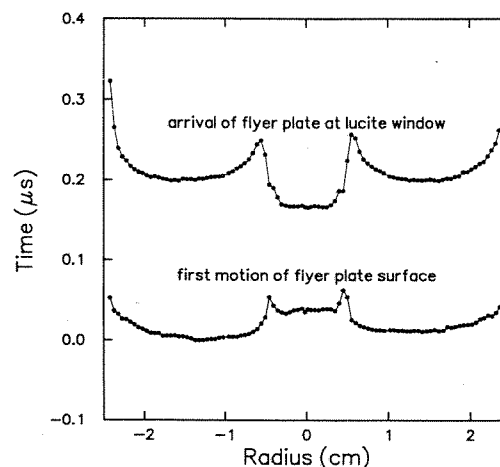


FIG. 9. Radial dependence of flyer plate timings.

the tube wall where it is delayed by about 6 nsec. Away from the boundaries, the detonation wave is also flat. At the shock tube wall, it lags by  $\sim 30$  nsec because of a rarefaction caused by the inward motion of the wall.

The signal from the axial shock arrives at the free surface of the flyer plate 30 nsec later than that of the bulk of the detonation wave. Assuming the incident wave speed is the detonation velocity, which for the hexane we justify below, it follows from the impedance match to the flyer plate that the detonation wave arrived at the front surface of the flyer plate 130 nsec earlier and the axial shock 117 nsec earlier. Therefore, at the end of the shock tube, the axial shock is 43 nsec behind the bulk of the detonation wave. This corresponds to an axial distance of 0.04 cm.

We note that the transit time for a radial signal from the detonation wave to the inside of the shock tube wall is 90 nsec. Thus even neglecting the delay of the detonation wave on the outside of the shock tube wall, the axial shock is ahead of the signal from the applied pressure pulse at the inside of the shock tube. The apparent delay of the axial shock near the shock tube wall is an artifact due to the shadowing effect of the shock tube wall in the transit of the signal through the flyer plate, and the axial shock is planar to the accuracy of the measurement.

The time difference across the flasher gap from Fig. 9 determines the free surface flyer plate velocity, which is shown in Fig. 10. The average free surface velocity of the flyer plate over the hexane is  $U_{FS} = 0.30$  cm/ $\mu$ sec. Behind the shock transmitted to the flyer plate the particle velocity is  $U_p = \frac{1}{2} U_{FS} = 0.15$  cm/ $\mu$ sec. This determines the shock speed  $U_s = 0.68$  cm/ $\mu$ sec and the shock pressure  $P_s = 0.79$  Mbar in the steel flyer plate. The incident hexane shock strength is determined by the impedance match, which results in the measured transmitted shock strength. Using the available Hugoniot data<sup>11</sup> one obtains for the state in the hexane behind the axial shock:  $U_p = 0.49$  cm/ $\mu$ sec,  $U_s = 0.88$  cm/ $\mu$ sec, and  $P_s = 0.29$  Mbar. Thus the axial shock velocity is the same as the detonation velocity. The shock has a Mach number of  $M = U_s / c_0 \approx 9$ .

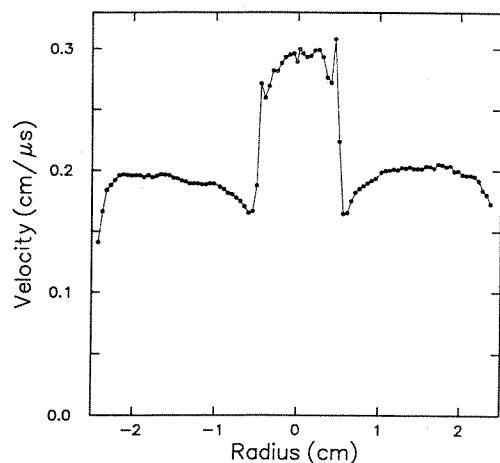


FIG. 10. Flyer plate velocity.

A duplicate phased implosion experiment with hexane (E-4947) was diagnosed with an x-ray pulser. The radiograph is shown in Fig. 11. The picture at the bottom is before the shot and at the top is after the detonation wave traveled 5.95 cm (7 diam) along the working portion of the shock tube. It is clearly seen that the minimum nozzle radius is a substantial fraction of the initial shock tube radius. This is an indication of the high pressure behind the axial shock.

#### IV. NUMERICAL CALCULATIONS

Simulating the phased implosion experiments with numerical calculations gives insight into the details of the fluid flow that cannot be experimentally measured. Here we describe 2-D calculations performed with the CAVEAT code<sup>12</sup> for the experiment with the hexane working fluid. The numerical results are compared with the experimental data. In addition, the asymptotic flow for the 2-D calculations is compared with that for the 1-D model in steady nozzle flow.

##### A. 2-D calculations

The CAVEAT calculations presented here use a finite difference algorithm on a quadrilateral mesh in cylindrical coordinates; radius and axial distance. The initial configuration for the 2-D calculation is shown in Fig. 12. CAVEAT treats the material boundaries as Lagrangian interfaces of an arbitrary Lagrangian-Eulerian mesh. Mesh points on the material interface can move tangentially to the interface to accommodate changes in the interior mesh. The approximate effect is to treat the radial flow with a Lagrangian mesh and the axial flow with an Eulerian mesh. This minimizes numerical errors caused by the large shear along the wall-fluid interface.

The HE is modeled with a JWL equation of state<sup>13</sup> and the detonation wave by a programmed burn. We note that the CJ pressure is 370 kbar and the detonation velocity is 0.88 cm/μsec. The steel wall and steel end plug are modeled using the SESAME equation of state tables,<sup>14</sup> material #4270. The equation of state of *n*-hexane is approximated by a Grüneisen EOS,<sup>15</sup> which is fit to data along the principal shock Hugoniot. The Hugoniot data<sup>11</sup> are well fit by a

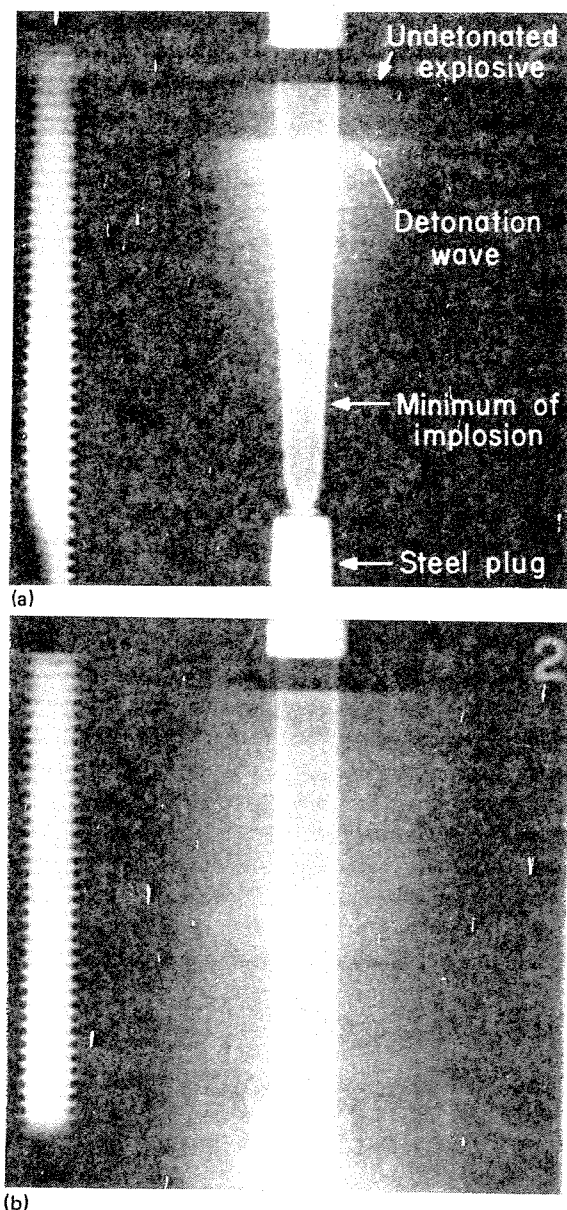


FIG. 11. Radiograph of the hexane phased implosion experiment. The space scale on the left is a rod with 1 mm wide grooves 1 mm apart. (a) dynamic, (b) static.

piecewise linear relationship between shock and particle velocity. A phase transition (chemical decomposition) occurs at approximately 200 kbar, indicated by a break in the data. The phase transition is of importance because the nozzle flow in the experiment crosses through this phase boundary. The Grüneisen coefficient is taken to be a piecewise linear function in  $V$ . The hexane EOS is specified in more detail in Appendix B.

A series of pressure contour plots of the working fluid showing the formation of the axial shock is shown in Fig. 13. The formation of the axial shock is affected by the presence of the steel end plug, as can be seen in the contour plot at  $t = 2.5 \mu\text{sec}$ . By  $t = 3.5 \mu\text{sec}$  the Mach configuration for the formation of the axial shock is clearly visible. An expanded view of this is shown in Fig. 14. At this stage the radial shocks play an important role in setting the working fluid on an adiabat with a high sound speed. This allows a compres-

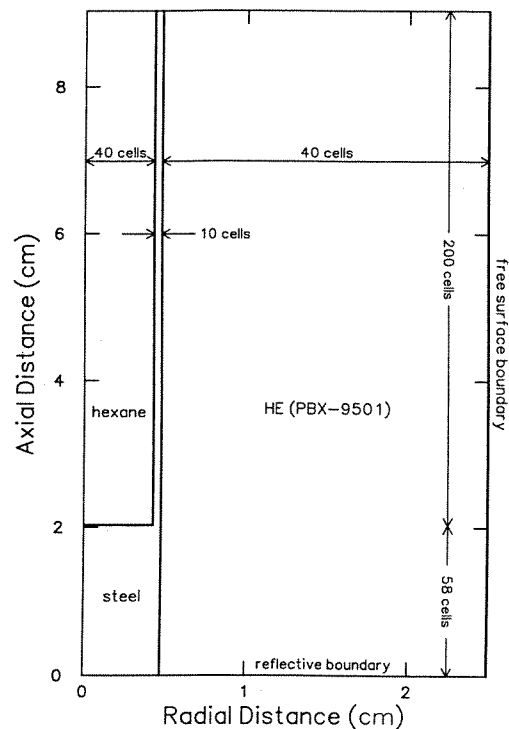


FIG. 12. Initial configuration for the CAVEAT calculation.

sive wave to overtake and interact with the Mach configuration moving the triple point radially outward. By  $t = 4.5 \mu\text{sec}$  the Mach stem has grown in radial extent to become the axial shock. At this time the flow behind the axial shock is approximately uniform in the radial direction. The adiabat of the working fluid is primarily set by the axial shock and the weaker radial shocks are not significant. After this time the flow is well described by the 1-D equations for flow in a

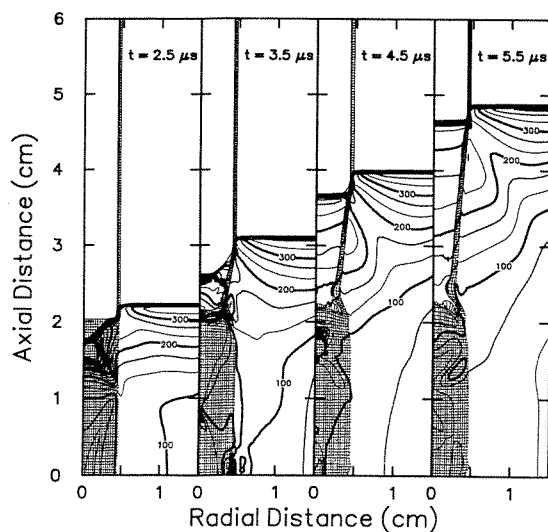


FIG. 13. Pressure contour plots showing the time evolution of flow in the working fluid;  $t = 2.5, 3.5, 4.5,$  and  $5.5 \mu\text{sec}$ . Contour levels are evenly spaced with the heavy lines in multiples of 100 kbar. The steel wall and end plug are shown as cross hatched.

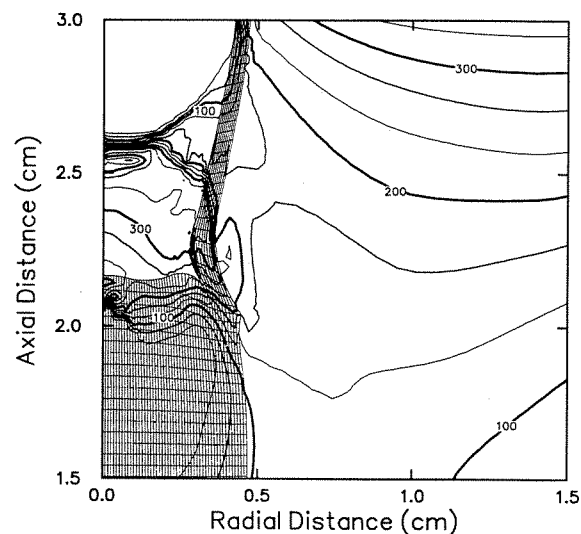


FIG. 14. Expanded view of the pressure contour plot at  $t = 3.5 \mu\text{sec}$  showing the Mach configuration. Contour levels are evenly spaced with the heavy lines in multiples of 100 kbar. The steel wall and end plug are shown as cross hatched.

duct of variable and time-dependent cross-sectional area, Eqs. (6)–(8).

In this calculation, the formation of the Mach stem results from the interaction of the phased implosion with the end plug and not the reflection of an oblique shock off the axis, as described in Sec. II A. This indicates that though the details may vary with the setup, the formation of an axial shock is not sensitive to initial conditions. However, the experimental details of the start-up are important to efficiently form an axial shock in a short distance.

The flow in the HE approaches an equilibrium configuration after the axial shock has formed and stabilized. A pressure contour plot at  $t = 9 \mu\text{sec}$  is shown in Fig. 15. Be-

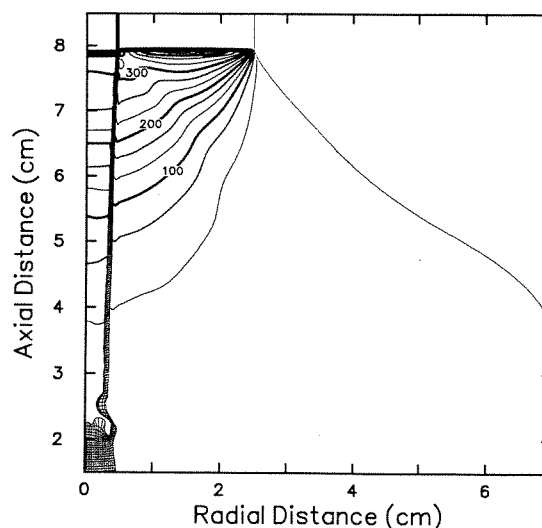


FIG. 15. Pressure contours at a time when the axial shock reaches the end of the shock tube,  $t = 9 \mu\text{sec}$ . Contour levels are evenly spaced with the heavy lines in multiples of 100 kbar. The steel wall and end plug are shown as cross hatched.

hind the detonation wave the outer surface of the HE has blown outward and a rarefaction wave propagates inward to the shock tube. The HE is thick enough for most of the effect from the outer boundary to occur behind the nozzle throat where it cannot affect the propagation of the axial shock. At the interface between the HE and the shock tube, the inward motion of the tube wall couples to the flow behind the detonation wave. This affects the pressure at the interface, which plays the role of the applied pressure pulse for the analysis in Sec. II. We also note that the phase velocity of the pressure pulse is the velocity of the detonation wave in the HE.

## B. Comparison with experiment

At the time of the radiograph for the hexane phased implosion experiment the detonation wave has traveled 6 cm from the plug at the start of the tube. The shape of the nozzle from the experiment and the calculation are in good agreement, as seen in Fig. 16, in which the digitized position of the wall from the radiograph (Fig. 11) is plotted together with the interface from the numerical calculation. The difference is probably due to uncertainties in the equations of state, and shear or strength properties in the metal wall (which is modeled as a fluid) as the pressure behind the detonation wave falls off.

A pressure contour plot at a time when the axial shock is close to the experimental end of the shock tube ( $\sim 5.9$  cm from the start of the plug) is shown in Fig. 15. This is to be compared with the data from the reflection change technique shown in Fig. 9. In both cases we see the axial shock is planar and is propagating slightly behind the detonation wave. The agreement is within the resolution of the calculation and the accuracy of the experimental measurements.

## C. Comparison with steady-state solution

The calculations show that the flow in the nozzle is approaching, but has not reached, steady state by the end of the experiment. The calculations were continued for about twice

the distance or until the axial shock had traveled 12 cm to allow a steady-state flow to be reached. The longer run used a coarser mesh with half the resolution. In the region of overlap the two calculations agreed well, indicating that the solution converged under mesh refinement. At 12 cm of run, we see in Fig. 17 that the converging section of the nozzle is about 2 cm long and that there is little radial dependence of the pressure within the nozzle. Behind the nozzle throat, the shock tube wall blows outward as the pressure behind the detonation falls off due to the Taylor wave and rarefaction from the outer boundary. In Fig. 18 the shape of the tube wall is shown relative to the detonation front at a sequence of times. This shows that the nozzle has converged to a steady-state shape  $t = 15 \mu\text{sec}$ . Also, at the time of the radiograph,  $t = 9 \mu\text{sec}$ , the shape of the nozzle has not reached steady state.

To compare with the steady-state theory, we solved the nozzle flow equations described in Sec. II B. We used the pressure profile along the HE/wall interface determined from the 2-D numerical simulation for the applied pressure pulse  $P_a$  of the 1-D model equations. As seen in Fig. 19, the pressure profile relative to the detonation front has converged to a time-independent profile  $\bar{P}_a$  by  $t = 15 \mu\text{sec}$ . At steady state, the axial shock moves with the detonation velocity.

The hexane isentrope in the  $P$ - $V$  plane through the shock state is shown in Fig. 20. We note that the discontinuous derivative corresponds to a phase transition. The magnitude of the jump of the slope depends on the Grüneisen coefficient in the EOS. Since there are no data for the Grüneisen coefficient in this regime of state space our choice leads to some uncertainty in the isentrope. Given the isentrope, the algebraic equations for the steady nozzle flow are easily solved.

The pressure in the nozzle as a function of cross-sectional area is shown in Fig. 21. If the jump in sound speed at the

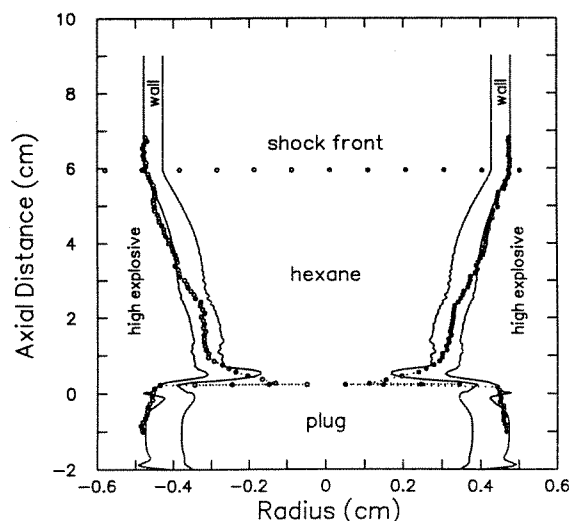


FIG. 16. Comparison of the nozzle shapes from experiment and calculation. Note, the scale is  $r:z = 1:10$ .

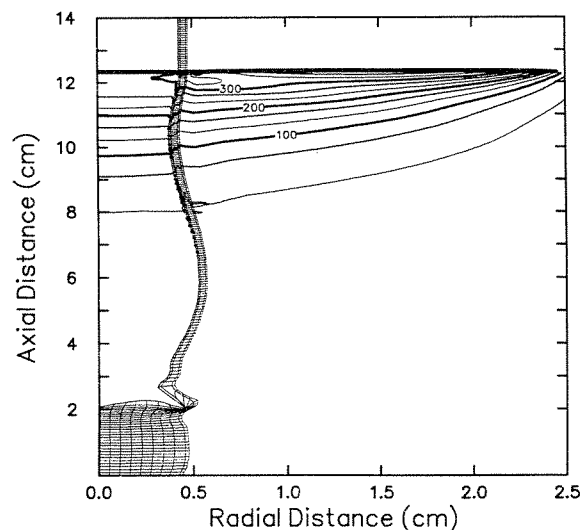


FIG. 17. Pressure contours when the flow reaches steady state,  $t = 14 \mu\text{sec}$ . Contour levels are evenly spaced with the heavy lines in multiples of 100 kbar. The steel wall and end plug are shown as cross hatched.

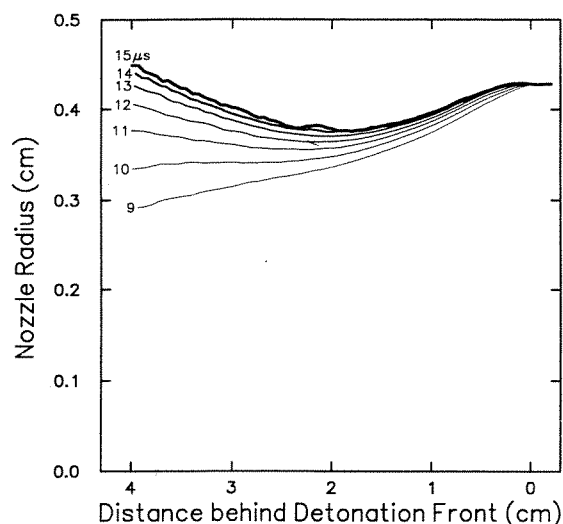


FIG. 18. The time sequence of nozzle shapes.

phase transition were large enough to cause the flow to change from subsonic to supersonic, then a second shock in the nozzle would be necessary for steady state. This does not occur for our choice of the Grüneisen coefficient used in the EOS.

We numerically solved the 1-D model for steady state, Eqs. (9) and (10), varying the shock position until the sonic boundary condition at the throat was achieved. Uncertainties in the equation of state drop out in a comparison to the 2-D calculation since the same equation of state is used in both cases. Moreover, the axial position is measured relative to the applied pressure pulse that is common to both calculations.

Figures 22 and 23 show the comparison between the 1-D steady-state and the 2-D asymptotic solution for the pressure profiles and nozzle shapes, respectively. We observe an excellent agreement in the pressure profiles. Both profiles

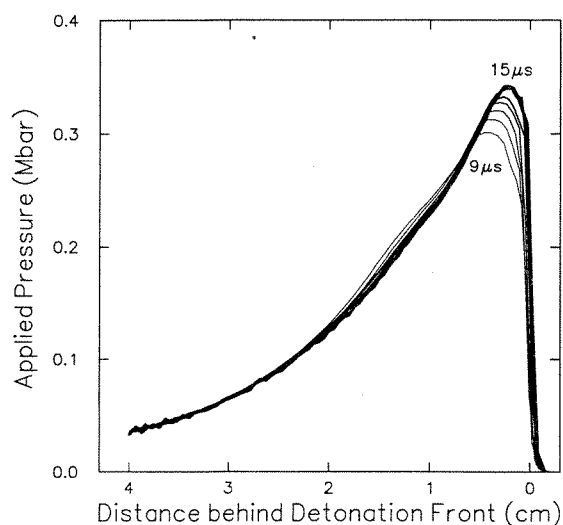


FIG. 19. The time sequence of applied pressure profiles.

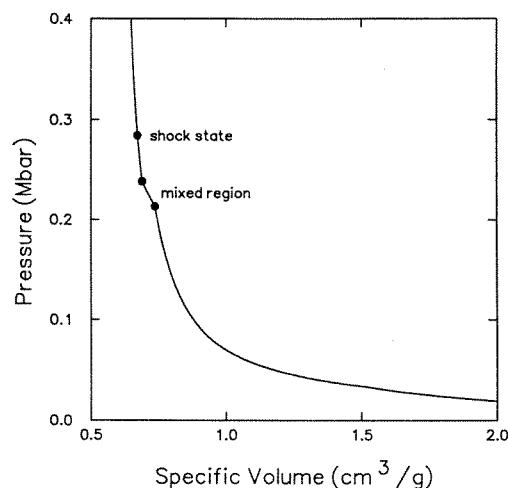


FIG. 20. Isentrope of *n*-hexane through the state shocked to the detonation velocity.

show a phase transition approximately 1 cm behind the shock front. The shock fronts are at the same position, but as expected, the shock is smeared out in the 2-D calculation. As can be seen from Fig. 23, the inside of the 2-D wall initially moves outward just as the mass layer does in the 1-D model. The agreement between the two shapes is within a small fraction of the total wall thickness. In both cases, the length of the nozzle ahead of the sonic point is approximately 2 cm. This confirms that the 1-D model accurately describes the steady state of the axially phased channel implosion and shows that the approximations made are indeed justified.

## V. DISCUSSION AND CONCLUSION

We have shown that an axially phased implosion of a channel can generate, propagate, and maintain a strong planar shock in a working fluid at higher pressures than a standard shock tube. The steady-state flow in the channel has several properties of practical and theoretical interest. Most importantly, theoretical considerations and numerical calculations indicate that a steady flow is reached for a wide

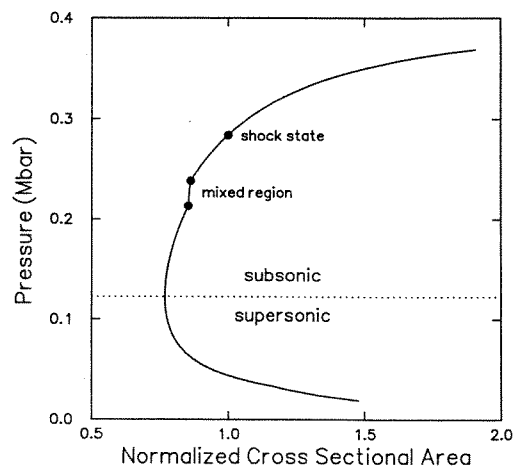


FIG. 21. Hexane pressure for steady nozzle flow.

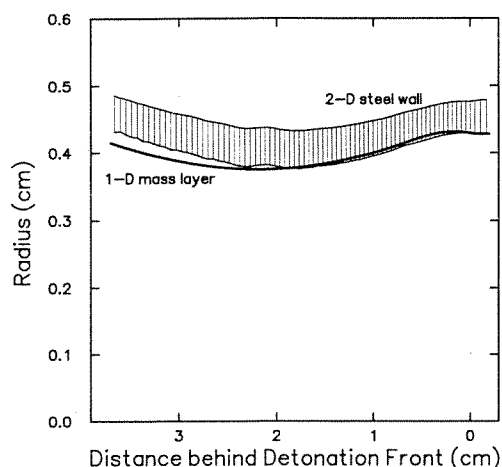


FIG. 22. Comparison of steady-state nozzle pressure with the 2-D calculation.

range of starting conditions and is stable. Moreover, the flow is not very sensitive to the cross-sectional shape of the channel.

The region behind the onset of the phased implosion forms a nozzle. The nozzle flow is well characterized: uniform across the channel, simple and predictable in the axial direction. The flow behind the nozzle throat has no effect on the shape of the converging section of the nozzle and the flow inside it.

These properties form the basis of an alternative shock tube design that is not limited in pressure by material strength of the tube wall. With high explosives driving the phased implosion, a super shock tube capable of reaching high pressures and energy densities is feasible. Experimentally we have demonstrated the possibilities of this approach with a simple design. Here the velocity of the phased implosion is equal to the detonation velocity of the explosive. As pointed out in Ref. 1 the velocity of the phased implosion can be made to exceed the detonation velocity. Rather than be-

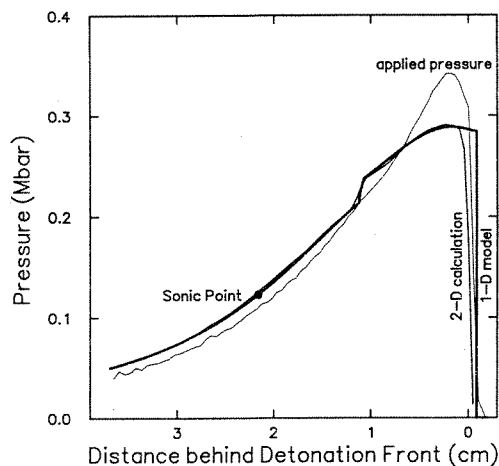


FIG. 23. Comparison of steady-state nozzle shape with the 2-D calculation.

ing limited by the detonation velocity the super shock tube is limited by the energy density and pressure of the high explosive.

The super shock tube extends to higher pressures and temperatures conventional shock tube applications of studying fluid flows and material properties. The design of the super shock tube with the shape of the nozzle as a new dynamical variable makes possible a new technique for extracting information on material properties and fluid flow. For steady-state flow, the shape of the nozzle determines the pressure difference across the tube wall. With a well characterized driving system this can be used to determine the equation of state of the working fluid along an isentrope behind the axial shock. The region of phase space that can be explored in this way is particularly relevant for the detonation products of high explosives.

The potential for high accuracy of super shock tube measurements is based on the fact that the pressure of the working fluid can be measured relative to the driver pressure or vice versa for calibration purposes. Calibration will involve experimental, theoretical, and numerical efforts to refine, for example, the equations of state of the driver detonation products and to capture quantitatively the deviations of the nozzle flow from its simple one-dimensional approximation. Frictional drag of the working fluid with the wall, primarily due to a turbulent boundary layer, affects the precise shape of the nozzle. However, any perturbation requires time to develop and usually will be swept out the back of the nozzle before it can develop to a size that significantly changes the nozzle flow. Comparison of experiments with different nozzle lengths or different cross-sectional areas may be used to study the growth of boundary layers and turbulent perturbations. The nozzle length may be varied by adjusting the wall mass per length of the shock tube.

In summary the super shock tube has the potential to develop into a tool to measure equations of state, address the dynamics of turbulent mixing and other hydrodynamical phenomena. The super shock tube is particularly well suited to the range of phase space, which is of interest in detonation phenomena.

Another application of an axially phased implosion of a shock tube is to benchmark hydrodynamic codes. Several features of the shock tube flow are well suited for testing hydrodynamics codes. The formation of the axial shock is a nontrivial two-dimensional flow. The flow evolves in time to a well characterized steady-state solution, which, even for nontrivial equations of state, may be accurately determined by solving ordinary differential equations. This is remarkable considering that the radial motion of the wall is an important dynamical degree of freedom and therefore makes the solution two dimensional. Moreover, we have shown that analytic solutions may be constructed. An accurate numerical calculation of the axial shock propagation depends on the proper treatment of the fluid-wall interface and in particular the strong shear layer. In addition, the gradient behind the axial shock makes the shock Hugoniot jump conditions sensitive to artificial numerical smearing of the shock. Since the flow inside the tube is sensitive to small differences between the shock velocity and the phase veloc-

ity, small numerical errors show up in the shape of the tube wall, the position of the axial shock relative to the onset of the applied pressure, and the axial profile of the flow behind the shock. These features of the flow can be used to discriminate among different numerical algorithms. Finally, the calculations can be validated by comparison with simple experiments such as described in this paper.

In addition to the potential applications, the channel flow of an axially phased implosion is of theoretical interest. Our experiments and calculations indicate that the steady-state flow is a stable attractor of the hydrodynamic equations with a large basin of attraction characterized by the initial and boundary conditions. We have given theoretical arguments to support this conjecture.

There is a strong similarity between the 1-D model equations for the axially phased implosion and the 1-D equations for reactive hydrodynamics with a single irreversible reaction. This leads to a striking similarity between their asymptotic solutions in the underdriven case; steady-state nozzle flow and CJ detonation wave. A detonation wave consists of a shock followed by a reaction zone, see e.g., Ref. 16. In the underdriven case, the reaction zone ends at a sonic point decoupling the reaction zone from the flow behind it. This is analogous to the nozzle region ahead of the throat for the phased implosion. In both cases energy is supplied to the fluid in the region behind the shock; the energy release by the chemical reaction corresponds to the energy supplied by the implosion, and the detonation velocity corresponds to the phase velocity. Also, the formation of the axial shock in the 1-D model, i.e., neglecting radial waves, is similar to a shock to detonation transition.<sup>17</sup> For detonation waves as well as the phased implosions, the hydrodynamical equations are coupled to one external degree of freedom, which satisfies an additional dynamical equation. For the detonation wave it is the burn fraction and for the axially phased implosion it is the cross-sectional area of the channel. This analogy may serve to carry over insights from one system to the other. For example, it is known that detonation waves are insensitive to the details of initiation and usually are stable attractors. However, for some parameters the steady detonation waves become unstable leading to a galloping detonation wave that oscillates about the steady-state solution.<sup>18-21</sup> This suggests the possibility of a "chugging" mode of the nozzle flow.

The parameter range for the axially phased implosion we have investigated is that in which the energy supplied by the driver can be matched to the energy required to drive the axial shock. Other parameter ranges are also of interest. Applications for the overdriven case, with a large excess of energy supplied, were discussed in Refs. 1 and 2. The underdriven case, in which the energy supplied is insufficient to drive an axial shock with the full cross-sectional area of the channel, is also important. The use of an optical fiber as a timing pin or pressure transducer, as discussed in Ref. 22, is an example. In this case the fiber is the channel and a shock in the surrounding medium is the source of the applied pressure pulse. When the density of the medium is lower than that of the fiber the axial shock is pressure limited and rides far back in the nozzle and two-dimensional effects invalidate our simple model. Thus it is of interest to extend our analysis

of the axially phased implosion to the overdriven and underdriven cases.

In summary, we have developed the theory for the steady-state flow of a supersonically phased channel implosion in the energy balanced regime. The theory predicts a stable planar axial shock followed by an isentropic nozzle flow. The theoretical predictions have been corroborated by a simple experiment. Numerical calculations show the formation of the axial shock during start-up and agree with experimental results and theory. Numerical simulations also show how the steady state is approached. A potentially important application of the axially phased implosion is the design of a super shock tube.

## ACKNOWLEDGMENT

This work was supported by the U.S. Department of Energy.

## APPENDIX A: EXISTENCE AND UNIQUENESS OF STEADY-STATE SOLUTION

In this appendix we analyze the 1-D model Eqs. (9) and (10) for the steady-state shape of the nozzle using the sonic boundary condition at the nozzle exit. We prove that a solution exists and that it is unique. The proof is based on the energy balance between the external energy supplied by the applied pressure pulse and the energy needed to drive the axial shock followed by the steady-state nozzle flow. We show that, as functions of the position of the axial shock relative to the nozzle entrance, the energy supplied is monotonically decreasing and the energy needed is monotonically increasing. Hence these two functions have exactly one intersection, which uniquely determines the shock position for the steady-state solution.

We assume  $\tilde{P}_a(t)$  is 0 for  $t < 0$ , rises discontinuously at  $t = 0$  and is monotonically decreasing for  $t > 0$ . In addition, we need to assume that  $\tilde{P}_a(t)$  falls off sufficiently fast. This additional condition is clarified below. For Eq. (10), the onset of the applied pressure pulse is at  $z = 0$ . Thus the shock is at the nozzle entrance and ahead of the onset of the applied pressure pulse if  $z_s > 0$ , and the shock is inside the nozzle and behind the onset if  $z_s < 0$ . We note that  $\tilde{P}_a(-z/v_\phi)$  decreases as  $z$  moves back into the nozzle, and that for  $z < z_s$ ,  $dP/dR > 0$ .

Equations (9) and (10) may be integrated backward into the nozzle, starting at the nozzle entrance,  $z_0 = 0$  if  $z_s < 0$  or  $z_0 = z_s$  if  $z_s > 0$ , with initial data  $R = R_0$  and  $U = 0$ . The integration is to be terminated at the first point  $z_i < 0$  where either  $U \geq 0$  (outward motion) and  $dU/dz < 0$  (outward acceleration), or where the critical radius for nozzle flow is reached and  $P_N$  becomes ill defined. The problem is to determine  $z_s$  such that the minimum  $R$  corresponds to the critical radius.

We start with two simple properties of the solution to Eqs. (9) and (10) for a fixed  $z_s$ . The first lemma guarantees that the termination point of the integration is always reached.



**Lemma 1:** For a given shock position  $z_s$ , the solution to Eqs. (9) and (10) for the shape of the wall  $R(z)$  either extends to the critical radius  $R_*$ , or has one local minimum of  $R$ , or is monotonically increasing.

*Proof:* If  $z_s > 0$  then either  $R$  is monotonically increasing or has a local maximum for  $z < 0$ . A minimum of  $R > R_*$  for  $z < 0$  occurs when  $U = 0$  and  $dU/dt > 0$ . Then from Eq. (10) we have,  $P(z) > \tilde{P}_a(-z/v_\phi)$ . As  $z$  decreases away from the minimum,  $P_N^{\text{sub}}$  increases and  $\tilde{P}_a$  decreases. Therefore, after the minimum,  $dU/dt$  and hence  $U$  remain positive, and  $R$  continues to increase.

From now on, we neglect the physically uninteresting case when the shock is ahead of and overwhelms the applied pressure pulse to the extent that  $R$  never gets less than  $R_0$ . Then, the termination point of the integration corresponds either to a local minimum in radius or the critical radius. We denote quantities at the termination point by the subscript  $t$ . The next lemma gives the critical equation used to determine the energy balance.

**Lemma 2:** The solution to Eqs. (9) and (10) satisfies

$$\frac{1}{2} \sigma U^2 = \int_{A_i}^{A_0} (\tilde{P}_a - P_N) dA. \quad (\text{A1})$$

*Proof:* The result follows from multiplying Eq. (10) by  $U$ , integrating from  $z_0$  to  $z$ , and then substituting with Eq. (19).

The problem is to determine  $z_s$  such that  $U(z_s) = 0$  and  $R(z_s)$  is the critical radius. This requires a balance between the energy needed to drive the steady-state flow in the nozzle,

$$\int_{A_i}^{A_s} P_N dA,$$

where  $A_s$  is the area of the shock front and  $A_i$  is the area at the sonic point, and the external energy supplied

$$\int_{A_i}^{A(0)} \tilde{P}_a dA,$$

where  $A(0)$  is the area at the onset of  $\tilde{P}_a$  and at  $A_i$  is the area minimum  $R$ .

The next proposition shows that the energy needed is a monotonically increasing function of the shock position.

**Proposition 1:** The energy needed to drive the steady-state flow in the nozzle decreases as  $z_s$  decreases.

*Proof:* Since  $P_N$  is a function of the area ratio we have

$$\int_{A_i}^{A_s} P_N dA = A_s \int_{A_i/A_s}^1 P_N \left( \frac{A}{A_s} \right) d \left( \frac{A}{A_s} \right). \quad (\text{A2})$$

The integral on the right-hand side of the equation depends only on the nozzle solution and is independent of  $z_s$ . Therefore the energy needed is proportional to  $A_s$  and decreases as the shock falls back into the nozzle.

The next two propositions show that the external energy supplied is a monotonically decreasing function of the shock position.

**Proposition 2:** If the shock is inside the nozzle,  $z_s < 0$ , then the external energy supplied increases as  $z_s$  decreases.

**Lemma 3:** Consider two solutions of Eqs. (9) and (10), denoted by subscripts 1 and 2, respectively, with the shock at

$z_s = z_1$  and  $z_s = z_2$ . If  $z_2 < z_1 < 0$  then  $R_2(z) < R_1(z)$  for  $z < z_1$ .

*Proof of Lemma 3:* When the shock is behind the onset of  $\tilde{P}_a$ , it follows from the ordinary differential equations (ODE's) that  $U(z) < 0$  for  $z > z_1$ . The two solutions are the same for  $z > z_1$ . Between the two shocks  $U_2 < U_1$ . Hence  $R_2 < R_1$  at  $z = z_2$ . For  $z < z_2$ , suppose that the two solutions for  $R$  first intersect at the point  $z_c$  and  $R(z_c) = R_c$ . The geometry implies  $U_1 \leq U_2$  at  $z = z_c$ . We show that this leads to a contradiction. Consider  $z$  as a function of  $R$  for the two solutions. It follows that  $z_1(R) < z_2(R)$  for  $R > R_c$ . Since  $\tilde{P}_a$  is monotonic we have

$$\int_{R_c}^{R_0} [\hat{P}_2(R) - \hat{P}_1(R)] R dR > 0, \quad (\text{A3})$$

where  $\hat{P}(R) = \tilde{P}_a(-z(R)/v_\phi)$ . Therefore the external energy supplied from the nozzle entrance to  $z = z_c$  is greater for the second solution than for the first. Furthermore, the energy needed is greater for the first solution than for the second,

$$\begin{aligned} A_{s1} \int_{A_i/A_{s1}}^1 P_N \left( \frac{A}{A_s} \right) d \left( \frac{A}{A_s} \right) \\ > A_{s2} \int_{A_i/A_{s2}}^1 P_N \left( \frac{A}{A_s} \right) d \left( \frac{A}{A_s} \right). \end{aligned} \quad (\text{A4})$$

It now follows from Lemma 2 that  $U_2 < U_1$  at  $z = z_c$ . This is a contradiction. Hence the two solutions cannot cross for  $z < z_2$  and  $R_2$  remains below  $R_1$ .

*Proof of Proposition 2:* Consider the two solutions occurring in the lemma. Using  $R_2 < R_1$ , the monotonicity of  $\tilde{P}_a$  and Eq. (A1) an argument similar to the one in the above lemma can be used to show that

$$\int_{R_{t2}}^{R_0} \hat{P}_2(R) R dR > \int_{R_{t1}}^{R_0} \hat{P}_1(R) R dR. \quad (\text{A5})$$

This implies the external energy increases as  $z_s$  decreases.

**Proposition 3:** If the shock is ahead of the onset of  $\tilde{P}_a$  then the external energy supplied increases as  $z_s$  decreases.

**Lemma 4:** Consider two solutions of Eqs. (9) and (10), denoted by subscripts 1 and 2, respectively, with the shock at  $z_s = z_1$  and  $z_s = z_2$ . If  $0 < z_2 < z_1$  then  $R_2(z) < R_1(z)$  for  $z < z_1$ .

*Proof of Lemma 4:* It is trivial to show that  $R_1 > R_2$  and  $U_1 > U_2$  at  $z = z_2$ . It follows from the ODE's and the monotonicity of  $P_N$  with  $R$  that  $P_1 > P_2$  and  $dU_1/dz < dU_2/dz$  continue to hold for  $z < z_2$ .

*Proof of Proposition 3:* Consider the two solutions occurring in the lemma. There are two cases. In the first,  $U_1(z_{t1}) = 0$ . From the previous lemma it follows that  $U_2(z_{t1}) < 0$  and hence  $z_{t2} < z_{t1}$ . Using Eqs. (A1) and (A2) and  $R(z_{t2})$ , it is easy to show that the energy supplied by  $\tilde{P}_a$  is greater for the second solution than for the first. In the second case, both solutions end at the critical radius. It follows from Lemma 4 that  $z_{t1} < z_{t2}$ , and  $U_2 < U_1$  at  $z = z_{t2}$ . We now need an assumption on the applied pressure pulse. Namely,  $\tilde{P}_a$  falls off sufficiently fast such that  $P_N > \tilde{P}_a$  as  $R$  approaches the critical radius. By increasing  $\sigma$ , the time scale for the implosion increases and the condition on the falloff can al-

ways be met, provided that  $\tilde{P}_a(t) \rightarrow P_0$  as  $t \rightarrow \infty$ . The assumption implies that the wall accelerates outward as  $z \rightarrow z_i$ . It then follows that  $0 > U_1(z_{i1}) > U_1(z_{i2}) > U_2(z_{i2})$ . Because the nozzle energy is the same for both solutions, Lemma 2 implies in this case that the energy supplied is linearly dependent on  $U^2$ . Hence the energy supplied by  $\tilde{P}_a$  is again greater for the second solution than for the first. Therefore the external energy supplied is an increasing function of  $z_s$ .

**Theorem:** There exists a unique  $z_s$  such that the solution of Eqs. (9) and (10) at the nozzle throat is sonic.

*Proof:* Consider the two limiting cases. When the shock is far back in the nozzle, for the solution of the ODE's, the energy supplied is a positive constant and the energy needed approaches 0. Hence the energy supplied is greater than the energy needed. For the shock far ahead of the onset of  $\tilde{P}_a$ , the energy needed is a positive constant and the energy supplied becomes negative when the internal pressure overwhelms the applied pressure and blows out the wall. Hence the energy needed is greater than the energy supplied. By continuity, for some  $z_s$  the two energies are balanced. Lemma 2 implies  $U = 0$  at  $z = z_i$  and the solution satisfies the sonic boundary condition. Because the energy supplied is monotonically decreasing with  $z_s$  and the energy needed is monotonically increasing with  $z_s$ , there is only one energy balanced solution.

## APPENDIX B: EQUATION OF STATE FOR NUMERICAL CALCULATIONS

In this section we specify the equations of state used in the numerical calculation for *n*-hexane and PBX-9501. For both materials we use a Grüneisen form of the EOS,

$$P(V, E) = P_{\text{ref}}(V) + (\Gamma/V)[E - E_{\text{ref}}(V)]. \quad (\text{B1})$$

Following Ref. 15, for the hexane, the experimental data for the principal shock Hugoniot is used as the reference curve. The shock Hugoniot can easily be specified by the coefficients for a linear fit of the shock velocity as a function of the particle velocity,

$$u_s = C + Su_p. \quad (\text{B2})$$

The shock jump condition for mass conservation gives

$$u_p(V) = C(1 - V/V_0)/[1 - S(1 - V/V_0)]. \quad (\text{B3})$$

From the other shock jump conditions we obtain

$$P_H(V) = P_0 + \rho_0 u_p u_s, \quad (\text{B4})$$

$$E_H(V) = E_0 + \frac{1}{2}(P_0 + P_H)(V_0 - V).$$

The experimental shock data<sup>11</sup> indicate a phase transition and the shock velocity may be expressed as a piecewise linear fit in the particle velocity. For lack of experimental data we also use a piecewise linear function for the Grüneisen coefficient. This is a slight modification of the form of the EOS for solids described in Ref. 23, Appendix C Sec. 4.A.1. The fit we use is in three parts.

(1) For the first phase,  $V_1 = 0.737 \leq V \leq V_0 = 1.522$  cm<sup>3</sup>/g,

$$C = 0.1579 \text{ cm}/\mu\text{sec} \quad \text{and} \quad S = 1.534,$$

$$\Gamma(V) = 1.0 \times (V/V_0).$$

(2) In the mixed region,  $V_2 = 0.689 \leq V \leq V_1 = 0.737$

TABLE I. EOS coefficients for PBX-9501.

$A = 8.524$
$B = 0.1802$
$C = 0.01207$
$R_1 = 4.55$
$R_2 = 1.30$
$\Gamma = 0.38$

cm<sup>3</sup>/g,  $P_{\text{ref}}$ ,  $E_{\text{ref}}$ , and  $\Gamma(V)$  vary linearly between their values at the transition points  $V_1$  and  $V_2$  of the pure phases.

(3) For the second phase,  $0.637 \leq V \leq V_2 = 0.689$  cm<sup>3</sup>/g,

$$C = 0.0993 \text{ cm}/\mu\text{sec} \quad \text{and} \quad S = 1.588,$$

$$\Gamma(V) = 0.722 \times (V/V_2).$$

The function  $\Gamma(V)$  is chosen to give reasonable values for the sound speed near the shock Hugoniot. This defines the EOS in the region of interest for the nozzle flow in the phased implosion experiment.

For the HE, an isentrope through the CJ state of the detonation products,  $V_{\text{CJ}} = 0.40$  cm<sup>3</sup>/g and  $P_{\text{CJ}} = 0.37$  Mbar, is used as the reference curve. We use a JWL equation to describe the isentrope<sup>13</sup>

$$P_s(V) = A \exp\left(-\frac{R_1 V}{V_0}\right) + B \exp\left(-\frac{R_2 V}{V_0}\right) + C \left(\frac{V_0}{V}\right)^{\Gamma+1}, \quad (\text{B5})$$

$$E_s(V) = \left[ \frac{A}{R_1} \exp\left(-\frac{R_1 V}{V_0}\right) + \frac{B}{R_2} \exp\left(-\frac{R_2 V}{V_0}\right) + \frac{C}{\Gamma} \left(\frac{V_0}{V}\right)^{\Gamma} \right] V_0^{-1}. \quad (\text{B6})$$

With units of Mbar, Mbar cm<sup>3</sup>/g, and cm<sup>3</sup>/g for  $P$ ,  $E$ , and  $V$ , respectively, the coefficients for PBX-9501 fit to cylindrical test data from Table 8-7 of Ref. 24, are given in Table I. The initial state is given by  $\rho_0 = 1.84$  g/cm<sup>3</sup>,  $P_0 = 0$ . The programmed burn uses a detonation velocity,  $D = 0.88$  cm/ $\mu$ sec.

<sup>1</sup>H. Waldron, E. Moore, G. Steel, and C. Godfrey, 5th Aerospace Science Meeting, New York, 1967 (unpublished).

<sup>2</sup>J. D. Watson, Physics International Co., Report No. PIFR-098, San Leandro, CA, 1969.

<sup>3</sup>C. Q. Lin and S. F. Shen, J. Fluid Mech. **157**, 265 (1985).

<sup>4</sup>R. Courant and K. Friedrichs, *Supersonic Flow and Shock Waves* (Interscience, New York, 1948).

<sup>5</sup>T. -P. Liu, Commun. Math. Phys. **83**, 243 (1982).

<sup>6</sup>T. -P. Liu, Arch. Rat. Mech. Anal. **80**, 1 (1982).

<sup>7</sup>P. Embid, J. Goodman, and A. Majda, SIAM J. Sci. Stat. Comput. **5**, 21 (1984).

<sup>8</sup>G. A. Miranda, "End-lit Cylinder Experiments Using Hexane For the Working Fluid: Informal Report on Shots E-4928 and E-4933," Los Alamos National Laboratory, Los Alamos, NM, March 1981 (unpublished).

<sup>9</sup>G. A. Miranda, Los Alamos National Laboratory, Report No. M3-QR-82-1, Los Alamos, NM, 1982.

<sup>10</sup>J. M. Walsh and R. H. Christian, Phys. Rev. **97**, 1544 (1955).

<sup>11</sup>R. D. Dick, J. Chem. Phys. **71**, 3202 (1979).

<sup>12</sup>F. L. Addessio, J. R. Baumgardner, J. K. Dukowicz, N. L. Johnson, B. A.

- Kashiwa, R. M. Rauenzahn, and C. Zemach, Los Alamos National Laboratory, Report No. LA-10613-MS, Los Alamos, NM, 1990.
- <sup>13</sup>E. L. Lee, H. C. Hornig, and J. W. Kury, Lawrence Livermore National Laboratory, Report No. UCRL-50422, Livermore, CA, 1968.
- <sup>14</sup>K. S. Holian, Ed., Los Alamos National Laboratory, Report No. LA-10160-MS, Los Alamos, NM, 1984.
- <sup>15</sup>M. Rice, R. McQueen, and J. Walsh, in *Solid State Physics Vol. 6*, edited by F. Seitz and D. Turnbull (Academic, New York, 1958), p. 1.
- <sup>16</sup>W. Fickett and W. Davis, *Detonation* (Univ. of California, Berkeley, CA, 1979).
- <sup>17</sup>J. Bdzil and A. Kapila, Los Alamos National Laboratory, Preprint No. LA-UR 89-1720, Los Alamos, NM, 1989.
- <sup>18</sup>J. Erpenbeck, *Phys. Fluids* **7**, 684 (1964).
- <sup>19</sup>W. Fickett and W. Wood, *Phys. Fluids* **9**, 903 (1966).
- <sup>20</sup>H. I. Lee and D. S. Stewart, *J. Fluid Mech.* **216**, 103 (1990).
- <sup>21</sup>A. Bourlioux, A. J. Majda, and V. Roytburd, "Theoretical and Numerical Structure for Unstable One-Dimensional Detonations," Princeton University, 1989 (preprint).
- <sup>22</sup>M. J. George, R. Menikoff, and L. R. Veaser, Los Alamos National Laboratory, Report No. LA-11148-MS, Los Alamos, NM, 1988.
- <sup>23</sup>C. L. Mader, *Numerical Modeling of Detonations* (Univ. of California, Berkeley, CA, 1979).
- <sup>24</sup>B. M. Dobratz and P. C. Crawford, Lawrence Livermore National Laboratory, Report No. UCRL-52997, Livermore, CA, 1985.